Imaging brain activity during seizures in freely behaving rats using a miniature multi-modal imaging system

ILIYA SIGAL,[1,2] MARGARET M. KOLETAR,[3] DENE RINGUETTE,[1] RAANAN GAD,[1,2] MELANIE JEFFREY,[4] PETER L. CARLEN,[1,4] BOJANA STEFANOVIC,[3,5] AND OFER LEVI[1,2,*]

[1]*Institute of Biomaterials and Biomedical Engineering, University of Toronto, 164 College Street, Toronto, ON M5S 3G9, Canada*
[2]*The Edward S. Rogers Sr. Department of Electrical and Computer Engineering, 10 King's College Road, Toronto, ON M5S 3G4, Canada*
[3]*Sunnybrook Research Institute, 2075 Bayview Avenue, Toronto, ON M4N 3M5, Canada*
[4]*Krembil Research Institute, 60 Leonard Avenue, Toronto, ON M5T 2S1, Canada*
[5]*Department of Medical Biophysics, University of Toronto, 2075 Bayview Avenue, Toronto, ON M4N 3M5, Canada*
[*]*ofer.levi@utoronto.ca*

Abstract: We report on a miniature label-free imaging system for monitoring brain blood flow and blood oxygenation changes in awake, freely behaving rats. The device, weighing 15 grams, enables imaging in a $\sim 2 \times 2$ mm field of view with 4.4 μm lateral resolution and $1 - 8$ Hz temporal sampling rate. The imaging is performed through a chronically-implanted cranial window that remains optically clear between 2 to > 6 weeks after the craniotomy. This imaging method is well suited for longitudinal studies of chronic models of brain diseases and disorders. In this work, it is applied to monitoring neurovascular coupling during drug-induced absence-like seizures 6 weeks following the craniotomy.

References and links

1. T. H. Schwartz, "Neurovascular coupling and epilepsy: hemodynamic markers for localizing and predicting seizure onset," Epilepsy Currents **7**, 91–94 (2007).
2. M. Suh, H. Ma, M. Zhao, S. Sharif, and T. H. Schwartz, "Neurovascular coupling and oximetry during epileptic events," Molecular Neurobiology **33**, 181–197 (2006).
3. H. K. Shin, A. K. Dunn, P. B. Jones, D. A. Boas, M. A. Moskowitz, and C. Ayata, "Vasoconstrictive neurovascular coupling during focal ischemic depolarizations," J. Cereb. Blood Flow Metab. **26**, 1018–1030 (2006).
4. H. Girouard and C. Iadecola, "Neurovascular coupling in the normal brain and in hypertension, stroke, and alzheimer disease," J. Appl. Physiol. **100**, 328–335 (2006).
5. W. Ou, I. Nissilä, H. Radhakrishnan, D. A. Boas, M. S. Hämäläinen, and M. A. Franceschini, "Study of neurovascular coupling in humans via simultaneous magnetoencephalography and diffuse optical imaging acquisition," NeuroImage **46**, 624–632 (2009).
6. T. Durduran and A. G. Yodh, "Diffuse correlation spectroscopy for non-invasive, micro-vascular cerebral blood flow measurement," NeuroImage **85**, 51–63 (2014).
7. A. Devor, A. K. Dunn, M. L. Andermann, I. Ulbert, D. A. Boas, and A. M. Dale, "Coupling of total hemoglobin concentration, oxygenation, and neural activity in rat somatosensory cortex," Neuron **39**, 353–359 (2003).
8. D. A. Boas and A. K. Dunn, "Laser speckle contrast imaging in biomedical optics," J. Biomed. Opt. **15**, 011109 (2010).
9. K. Masamoto and I. Kanno, "Anesthesia and the quantitative evaluation of neurovascular coupling," J. Cereb. Blood Flow Metab. **32**, 1233–1247 (2012).
10. H. Yu, J. Senarathna, B. M. Tyler, N. V. Thakor, and A. P. Pathak, "Miniaturized optical neuroimaging in unrestrained animals," NeuroImage **113**, 397–406 (2015).
11. P. Miao, H. Lu, Q. Liu, Y. Li, and S. Tong, "Laser speckle contrast imaging of cerebral blood flow in freely moving animals," J. Biomed. Opt. **16**, 090502 (2011).

12. J. Senarathna, K. Murari, R. Etienne-Cummings, and N. Thakor, "A miniaturized platform for laser speckle contrast imaging," IEEE Trans. Biomed. Circuits Syst., **6**, 437–445 (2012).

13. R. Liu, Q. Huang, B. Li, C. Yin, C. Jiang, J. Wang, J. Lu, Q. Luo, and P. Li, "Extendable, miniaturized multi-modal optical imaging system: cortical hemodynamic observation in freely moving animals," Opt. Express **21**, 1911–1924 (2013).

14. H. Lu, P. Miao, Q. Liu, Y. Li, and S. Tong, "Dual-modal (OIS/LSCI) imager of cerebral cortex in freely moving animals," in "Photonics and Optoelectronics Meetings 2011," (SPIE, 2012), p. 83290P.

15. H. Levy, D. Ringuette, and O. Levi, "Rapid monitoring of cerebral ischemia dynamics using laser-based optical imaging of blood oxygenation and flow," Biomed. Opt. Express **3**, 777–791 (2012).

16. A. Edelstein, M. Tsuchida, N. Amodaj, H. Pinkard, R. Vale, and N. Stuurman, "Advanced methods of microscope control using μManager software," J. Biol. Methods **1**, e10 (2014).

17. Z. Luo, Z. Yuan, Y. Pan, and C. Du, "Simultaneous imaging of cortical hemodynamics and blood oxygenation change during cerebral ischemia using dual-wavelength laser speckle contrast imaging," Opt. Lett. **34**, 1480–1482 (2009).

18. S. J. Kirkpatrick, D. D. Duncan, and E. M. Wells-Gray, "Detrimental effects of speckle-pixel size matching in laser speckle contrast imaging," Opt. Lett. **33**, 2886–2888 (2008).

19. R. Mostany and C. Portera-Cailliau, "A craniotomy surgery procedure for chronic brain imaging," J. Vis. Exp. **18**, e680 (2008).

20. A. Y. Shih, J. D. Driscoll, P. J. Drew, N. Nishimura, C. B. Schaffer, and D. Kleinfeld, "Two-photon microscopy as a tool to study blood flow and neurovascular coupling in the rodent brain," J. Cereb. Blood Flow Metab. **32**, 1277–1309 (2012).

21. D. A. Dombeck, A. N. Khabbaz, F. Collman, T. L. Adelman, and D. W. Tank, "Imaging large-scale neural activity with cellular resolution in awake, mobile mice," Neuron **56**, 43–57 (2007).

22. B. B. Scott, C. D. Brody, and D. W. Tank, "Cellular resolution functional imaging in behaving rats using voluntary head restraint," Neuron **80**, 371–384 (2013).

23. J. T. Cole *et al.*, "Craniotomy: true sham for traumatic brain injury, or a sham of a sham?" J. Neurotrauma **28**, 359–369 (2011).

24. R.-Q. Huang, C. L. Bell-Horner, M. I. Dibas, D. F. Covey, J. A. Drewe, and G. H. Dillon, "Pentylenetetrazole-induced inhibition of recombinant γ-aminobutyric acid type A ($GABA_A$) receptors: mechanism and site of action," J. Pharm. Exp. Ther. **298**, 986–995 (2001).

25. A. Pitkänen, P. A. Schwartzkroin, and S. L. Moshé, *Models of Seizures and Epilepsy* (Academic Press, Burlington, MA, USA, 2005).

26. M. A. Cortez, G. K. Kostopoulos, and O. C. Snead, "Acute and chronic pharmacological models of generalized absence seizures," J. Neurosci. Methods **260**, 175–184 (2015).

27. B. Keogh, D. Cordes, L. Stanberry, B. Figler, C. Robbins, B. Tempel, C. Green, A. Emmi, K. Maravilla, and P. Schwartzkroin, "BOLD-fMRI of PTZ-induced seizures in rats," Epilepsy Research **66**, 75–90 (2005).

28. T. Zhang, J. Zhou, R. Jiang, H. Yang, P. R. Carney, and H. Jiang, "Pre-seizure state identified by diffuse optical tomography," Scientific Reports **4**, 3789 (2014).

29. B. Wang, J. Xiao, and H. Jiang, "Simultaneous real-time 3D photoacoustic tomography and EEG for neurovascular coupling study in an animal model of epilepsy," J. Neural Eng. **11**, 046013 (2014).

30. G. Casella and R. L. Berger, *Statistical Inference*, 2nd ed. (Duxbury Press, Pacific Grove, CA, USA, 2002).

31. R. P. Shockley and J. C. LaManna, "Determination of rat cerebral cortical blood volume changes by capillary mean transit time analysis during hypoxia, hypercapnia and hyperventilation," Brain Research **454**, 170–178 (1988).

32. A. K. Dunn, A. Devor, H. Bolay, M. L. Andermann, M. A. Moskowitz, A. M. Dale, and D. A. Boas, "Simultaneous imaging of total cerebral hemoglobin concentration, oxygenation, and blood flow during functional activation," Opt. Lett. **28**, 28–30 (2003).

33. A. K. Dunn, A. Devor, A. M. Dale, and D. A. Boas, "Spatial extent of oxygen metabolism and hemodynamic changes during functional activation of the rat somatosensory cortex," NeuroImage **27**, 279–290 (2005).

34. D. A. Boas, G. Strangman, J. P. Culver, R. D. Hoge, G. Jasdzewski, R. A. Poldrack, B. R. Rosen, and J. B. Mandeville, "Can the cerebral metabolic rate of oxygen be estimated with near-infrared spectroscopy?" Phys. Med. Biol. **48**, 2405–2418 (2003).

35. A. Devor, I. Ulbert, A. K. Dunn, S. N. Narayanan, S. R. Jones, M. L. Andermann, D. A. Boas, and A. M. Dale, "Coupling of the cortical hemodynamic response to cortical and thalamic neuronal activity," Proc. Natl. Acad. Sci. U.S.A. **102**, 3822–3827 (2005).

36. N. Harel, S.-P. Lee, T. Nagaoka, D.-S. Kim, and S.-G. Kim, "Origin of negative blood oxygenation level–dependent fMRI signals," J. Cereb. Blood Flow Metab. **22**, 908–917 (2002).

37. M. Murayama, E. Pérez-Garci, H.-R. Lüscher, and M. E. Larkum, "Fiberoptic system for recording dendritic calcium signals in layer 5 neocortical pyramidal cells in freely moving rats," J. Neurophysiol. **98**, 1791–1805 (2007).

38. B. A. Flusberg, A. Nimmerjahn, E. D. Cocker, E. A. Mukamel, R. P. Barretto, T. H. Ko, L. D. Burns, J. C. Jung, and M. J. Schnitzer, "High-speed, miniaturized fluorescence microscopy in freely moving mice," Nat. Methods **5**, 935–938 (2008).

39. W. Piyawattanametha, E. D. Cocker, L. D. Burns, R. P. Barretto, J. C. Jung, H. Ra, O. Solgaard, and M. J. Schnitzer, "In vivo brain imaging using a portable 2.9 g two-photon microscope based on a microelectromechanical systems scanning mirror," Opt. Lett. **34**, 2309–2311 (2009).

40. J. Sawinski, D. J. Wallace, D. S. Greenberg, S. Grossmann, W. Denk, and J. N. Kerr, "Visually evoked activity in cortical cells imaged in freely moving animals," Proc. Natl. Acad. Sci. U.S.A. **106**, 19557–19562 (2009).
41. K. K. Ghosh, L. D. Burns, E. D. Cocker, A. Nimmerjahn, Y. Ziv, A. El Gamal, and M. J. Schnitzer, "Miniaturized integration of a fluorescence microscope," Nat. Methods **8**, 871–878 (2011).
42. A. Osman, J. H. Park, D. Dickensheets, J. Platisa, E. Culurciello, and V. A. Pieribone, "Design constraints for mobile, high-speed fluorescence brain imaging in awake animals," IEEE Trans. Biomed. Circuits Syst. **6**, 446–453 (2012).

1. Introduction

Monitoring neurovascular coupling (NVC), or the response of the brain vasculature to the changes in neuronal activity, is key to understanding various brain diseases and disorders such as epilepsy [1, 2], stroke [3], and Alzheimer's disease [4]. NVC, which can also serve as surrogate to neuronal activity, can be monitored by a wide range of optical techniques that measure changes in brain blood flow and oxygenation, including Diffuse Optical Tomography (DOT) [5], Diffuse Correlation Spectroscopy (DCS) [6], Intinsic Optical Signal Imaging (IOSI) [7], and Laser Speckle Contrast Imaging (LSCI) [8]. A common challenge in monitoring NVC in animal disease models is the presence of anaesthesia, which confounds NVC [9], strongly perturbs neuronal activity, cerebral blood flow, cerebral metabolic rate of oxygen consumption, and prevents neuroimaging during animal behavior.

In response to the aforementioned challenge, significant effort has been made to miniaturize brain imaging systems that are mounted on, or implanted in, rodents' heads [10, and references therein]. Most such systems were designed to image fluorescently-labeled neuronal activation or ion dynamics, and relatively few studies showed *in-vivo* imaging of vascular dynamics in awake rat brains. Works by Miao, *et al.*, [11] and Senarathna, *et al.*, [12] used LSCI to image cortical blood flow speeds. Liu, *et al.*, [13] and Lu, *et al.*, [14] combined LSCI with IOSI for simultaneous measurement of cortical blood flow speeds and changes in oxygenated and deoxygenated hemoglobin (HbO and HbR, respectively) concentrations in tissue and vessels.

The chief limitation of these methods is the lack of a chronic optical access to the brain, as either a thinned skull window was used [11, 12, 14], or the skull was removed and the dura matter was left unprotected [13]. Imaging through a thinned skull in rats has two key limitations. Firstly, imaging sessions are limited to a few hours after device implantation, since the thinned bone becomes cloudy due to the inflammatory response. Secondly, differentiating the dura matter vessels from the cortical ones becomes challenging, thus confounding vascular analysis. These drawbacks limit the use of the reported devices to acute models of pathologies. Furthermore, the results shown had low spatio-temporal resolution with limited dynamic range due to a) the static scattering from the thinned skull and dura matter, and b) the limited spatial resolution of the imaging chips used. In addition, the use of the fiber bundle by Liu, *et al.*, required a modified temporal speckle imaging method for blood flow speed estimation, limiting temporal resolution.

In this paper we demonstrate a novel head-mounted device for wide field imaging of brain blood flow and brain blood oxygenation changes in awake, freely-moving rats with high spatio-temporal resolution, using a chronically-implanted cranial window. We sought to optimize both surgical protocol and device engineering to address the needs of neurophysiologists working on chronic models of brain diseases and disorders. Our cranial implant remains optically clear between 2 and > 6 weeks after surgery, providing access to the cortical surface, and thus permitting high spatio-temporal resolution multi-modal imaging of cortical hemodynamics. As a demonstration, we used our system to image changes in cortical hemodynamics in a drug-induced absence-like seizure model, showing longitudinal chronic recording capability suitable for drug discovery studies.
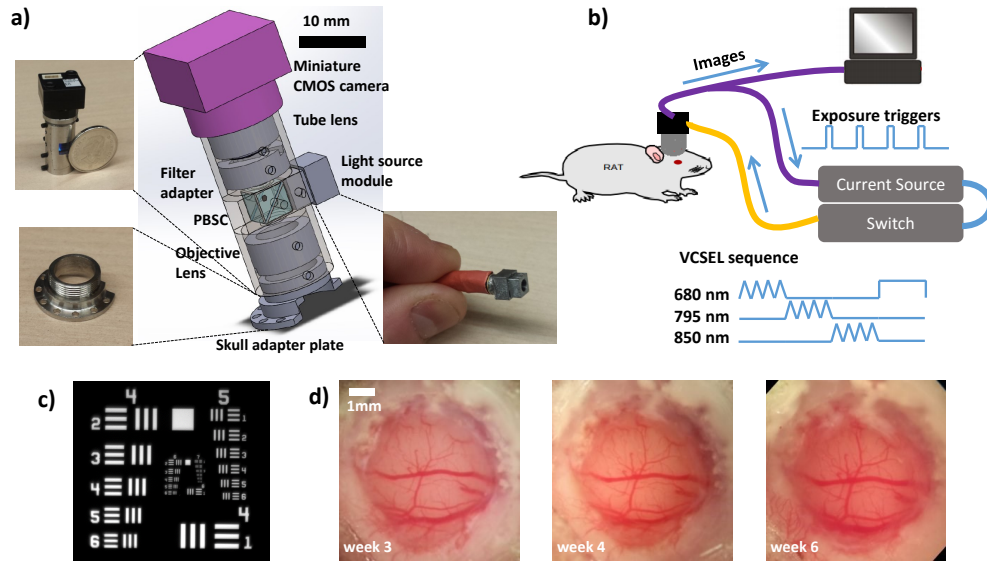
Fig. 1. Miniature head-mounted imaging system for monitoring rat brain hemodynamics. a) Device schematic. Insets: the imaging tube (top left), skull adapter plate (bottom left), and the light source module (bottom right). b) System diagram. c) Image of a USAF resolution target: computed contrast values are 11.5% at 161 lp/mm, 15% at 144 lp/mm, 19% at 128 lp/mm. d) Brain imaged through the chronic cranial window.

2. Methodology

In this section we describe our miniature imaging system design and characterization, the implantation of a chronic skull window, and our choice of a drug-induced seizure model to showcase the longitudinal study capability of our proposed method.

2.1. Optical imaging system

A schematic of our imaging device is shown in Fig. 1(a). The device consists of three components: the skull adapter plate, the imaging tube, and the light source module. The skull adapter plate is surgically adhered to the skull using three tapping screws, cyanoacrylate glue, and dental cement. The adapter plate is threaded to accept the imaging tube, and it is the only element of our system that is permanently attached to the rat; the imaging tube is attached during imaging.

The imaging tube houses two $f = 10.2$ mm focal length triplet imaging lenses (TRH064-010-A, Thorlabs Inc., Newton, NJ, USA), resulting in 1× magnification. The 3 mm wide aperture stop in our system results in $f/3.4$. A polarizing beam-splitter cube (PBSC, PBS052, Thorlabs Inc., Newton, NJ, USA) is placed between the imaging lenses to direct the (linearly polarized) illumination onto the brain tissue, and to separate the multiply-backscattered light from the undesired specularly-reflected light.

The light source module consists of four Vertical Cavity Surface Emitting Lasers (VCSELs, Vixar Inc., Plymouth, MN, USA), all mounted onto a single TO-46 package. VCSEL wavelengths are 680 nm (2×), 795 nm, and 850 nm, allowing mapping of HbO and HbR using a method described earlier [15]. The standard TO-46 package cap is replaced with a custom threaded cap, which is mated to the imaging tube using an adapter (Light Source Module in the schematic). Such design permits aligning the input polarization of the VCSELs to the polarization reflected by the PBSC. The VCSELs are tethered to a programmable current source and switch (Models

6221 and 7001 respectively, Keithley Instruments, Cleveland, OH, USA), as depicted in Fig. 1(b). Typical illumination power from a single VCSEL is 2–5 mW.

As discussed earlier [15], VCSELs present an attractive light source for multi-modal neural imaging due to the ability to change the emitters' coherence by modulating the driving current. Driving the lasers using a constant current, slightly above lasing threshold, produces highly coherent, single-mode illumination. Conversely, rapidly sweeping the driving current produces LED-like illumination with significantly reduced speckle. The high-coherence illumination mode is well suited for LSCI, while the low-coherence illumination mode is well suited for IOSI.

A miniature rolling-shutter CMOS camera (XiMu, Ximea Inc., Golden, CO, USA), utilizing an Aptina MT9P031 imaging chip, is used to collect the imaging data. Camera pixel pitch is 2.2 μm, with linear pixel well depth of ~8,500 electrons, digitized to 12 bits. To ensure adequate dynamic range and increase acquisition frame rate, 2×2 hardware binning was used during acquisition. Typically-sized 560×560 binned pixel-wide regions of interest (ROIs) were acquired at free-run speeds of ~ 24 Hz. The fast response time of the VCSELs allows for a rapid leap-frog image acquisition routine, as depicted in Fig. 1(b). The camera's exposure triggers are used to sequentially change the VCSELs that are illuminating the brain tissue, resulting in an effective acquisition rate of ~ 6 Hz utilizing all four illumination modes. While three wavelengths are available, typically only 680 nm and 795 nm were used, as only two wavelengths are needed to solve for the separate contributions of HbO and HbR. This is done to increase acquisition rate. The imaging results shown in this work use temporal averaging of 8 frames, with an effective 1 Hz sampling rate. Such sampling rate is sufficient for detecting seizures that are several seconds long, while still providing adequate signal-to-noise ratio (SNR).

Micro-Manager software [16] was used for image acquisition, while a custom Python program was used for separating the data channels in a post-processing step, and for computing LSCI flow speed maps and changes in HbO and HbR concentration, following the method described in reference [17].

The optical resolution of our system was limited by the camera pixel pitch. Fig. 1(c) shows an image of a USAF resolution target; we observe 20% contrast at a resolution of 128 line pairs per mm, more than sufficient for resolving capillary-sized vessels. The field of view of the imaging system is ~2 mm, limited by a) spot size of the projected illumination onto the brain, and b) depth of field of the imaging system (~ 100 μm), which renders off-center vessels out of focus due to the natural curvature of the brain surface. The speckle size in our system is 11 μm [18], which is more than double our effective (binned) pixel size of 4.4 μm, so that the Nyquist sampling criterion is satisfied for LSCI.

The weight of the entire device, including the base plate, is 15 grams, representing < 5% of the total body weight of the rat (typically 350-400 g). The weight of the device, and more importantly, the torque applied to the rat's head from the combined weight of the device and light-weight wires, is sufficiently low to avoid discomfort to the animal and allow normal behavior patterns (see Visualization 1).

2.2. Surgical preparation

A key feature of our approach is the incorporation of a custom stainless steel adapter plate with a chronic cranial window, facilitating the ability to record images over several weeks. All surgical and imaging procedures were performed in accordance with protocols approved by the Animal Care Committee at Sunnybrook Health Sciences Centre. Experiments were conducted on healthy, male Sprague-Dawley rats (weight 250 g at time of surgery), housed in standard ventilated cages on a 12:12 light/dark hour cycle with food and water provided *ad libitum*. Surgeries were conducted under strict sterile technique defined by the institutional veterinary standard operating procedure. The implantation of a chronic cranial window was translated from previous surgical descriptions in the mouse [19, 20] and rat [20], to incorporate the innovation of the optical
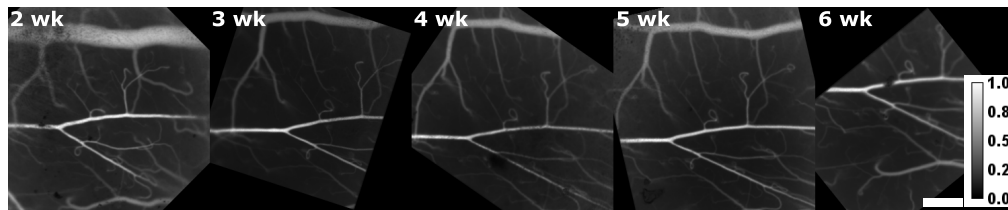
Fig. 2. LSCI-derived relative flow speed maps in a rat, imaged through a chronic cranial window. Each tile depicts a flow speed map imaged weekly, from 2nd to 6th week following a craniotomy. The flow speeds in the arterial and parenchymal regions vary within ±10% across 5 weeks of measurement. Scale bar is 0.5 mm.

adapter plate. Similar procedures for longitudinal imaging over > 1 week in awake rodents have been reported in the mouse by Dombeck, *et al.* [21], and also attained in the awake rat by Scott, *et al.* [22]. The rat was anesthetized with isoflurane, and administered dexamethasone (anti-inflammatory), buprenorphine (analgesic), and enrofloxacin (antibiotic). The top of the head was shaved and cleaned with isopropyl alcohol followed by an iodine solution. After an incision in the scalp, the skull surface was cleaned and muscle tissue was gently separated along the right lateral edge of the skull. A 6 mm wide cranial window was opened using a dental drill, and the dura layer was removed. 1% Agarose gel was deposited on the cortical surface and an 8 mm diameter cover slip placed over the agarose gel, making contact with the skull to maintain intra-cranial pressure. An air-tight seal around the cover slip was made using cyanoacrylate glue. The skull adapter plate was mounted on top of the cover slip using tapping screws and secured further with cyanoacrylate glue, followed by application of dental cement. The skull adapter plate did not make physical contact with the cover slip, but rather provided a platform above the cranial window onto which the imaging tube was secured. Carprofen (anti-inflammatory) was administered for three days post-surgery. Daily inspection of the implant and gentle acclimation to the imaging chamber was provided throughout the recovery period. The rat was allowed two weeks recovery for healing after inherent post-surgical inflammatory response [23], and to ensure secure attachment of the adapter plate to the skull prior to initiating the awake imaging paradigm. Following a 2 week-long refractory recovery period, during which imaging ability is limited, the window remained optically clear for > 6 weeks after implantation (see Fig. 2), allowing for chronic, longitudinal studies to be performed in freely behaving rats.

2.3. Seizure model

We imaged hemodynamic activity during absence-like seizures induced using the drug Pentylenetetrazol (PTZ) to showcase the ability of our device to image cerebrovascular response to neuronal activity longitudinally. PTZ is a commonly used $GABA_A$ receptor antagonist [24, 25]. Its mechanism of action is based on allesteric modulation of Cl^- channel activity. At low doses (20-30 mg per kg of body weight, dissolved in 0.9 g/L NaCl sterile saline, administered via intraperitoneal (IP) injection) it results in absence-like seizures that originate in the thalamus and spread to the cortex [25, 26]. This absence-like seizure has a well characterized and easily discernible motor response, namely depressed breathing, behavioral rest, and chewing (see Visualization 2). It has been shown to elicit hymodynamic response measured on BOLD-fMRI [27], DOT [28], and photoacoustic tomography (PAT) [29].

We chose this absence-like seizure model for two reasons: firstly, it allowed us to visually estimate seizure onset without electroencephalogram (EEG) electrodes. Secondly, absence seizures are the most common type of seizure in children and infants, and the PTZ model is commonly used in pharmacological testing of seizure rescue drugs.

2.4. Experimental procedure

Prior to attaching the imaging tube, the rat was anesthetized using 2% isoflurane. The cranial window was cleaned from debris using a lens cleaning tissue and ethanol. The imaging tube was screwed onto the skull adapter plate, and the image stream from the camera was used to estimate location of best focus by carefully rotating the imaging tube about the threads on the skull adapter plate. Once the location of best focusing of the brain was found, the imaging tube was secured to the skull adapter plate using two setting-screws. The procedure typically took between 5 and 10 minutes to complete. The rat was then placed inside the imaging chamber, and was allowed to recover from the effects of anesthesia. The recovery phase typically lasted for 5 minutes. Following recovery, "baseline" (prior to PTZ injection) activity was recorded for ~ 5 minutes. Following the "baseline" recording, the rat was removed from the cage, and was secured on its side. PTZ was dissolved in sterile saline (0.9% NaCl), at a concentration of 20 mg/mL. A bolus of the solution, at 20 mg/kg body weight, was delivered via an IP injection. Imaging data was recorded throughout the injection. The rat was then returned to the imaging chamber, and was visually monitored for signs of seizure. A video recording using a commercial-grade camera (Nikon Coolpix AW100) registered motor behavior, and was synchronized to the miniature camera recording with precision of ~ 0.5 s. Imaging sessions typically lasted for 30 minutes, after which the rat was anesthetized using 2% isoflurane and the device was removed from its head. The rat was monitored for 1 hour after the imaging session to ensure complete recovery.

3. Results

The imaging experiment took place 6 weeks (42 days) after the surgical implantation of the cranial window. The rat weighed 388 g at the time of imaging. The volume of injected PTZ solution was 0.39 mL. Figure 3(a) shows the rat, with the device attached on its head, exploring the imaging chamber. A map of the flow speeds, measured using LSCI, is shown in Fig. 3(b). Several arteries and veins are visible in the field of view. Highlighted in the flow map are the artery, vein, and parenchymal regions used for subsequent time-course analysis. Figures 3(c-d) show time-course of PTZ-induced seizures as manifested in changes in blood flow and blood oxygenation, illustrating the progression over the imaging session. The blood flow speeds were normalized to the mean baseline value, between $t = -6$ min and $t = -2$ min, prior to PTZ injection. The vertical dashed line at t = −1.8 min marks the time when the rat was physically picked up from the imaging chamber. The large increase in flow, combined with the sharp increase of venous HbO concentration is indicative of the sympathetic nervous response of the rat to being physically manipulated (see Fig. 7 in the Appendix for a control experiment showing increase in flow and HbO concentration and decrease in HbR concentration during handling followed by a sham injection of saline). The dashed line at t = 0 min marks the time when the syringe needle was inserted into the rat's abdominal cavity, inducing additional increase in flow and venous HbO concentration. Following the sustained increase in blood flow and HbO, there appears to be a depression in both. This is likely a result of exhaustion due to prolonged period of vasodilation. Once seizures commence (greyed regions in Fig. 3(c-d)), we see a slow increase in flow and increase in HbR to HbO ratio.

Following this initial response, we observed intermittent seizure-like events characterized by motor arrest for up to 20 minutes after injection. The hemodynamic response in this time frame is shown in Fig. 4(a-c), plotted separately for artery, vein, and the parenchymal region.

We quantified the changes in the hemodynamic response at onset of seizure-like events by performing motor arrest-onset locked averaging of the time courses. The resulting time traces, shown in Fig. 5, represent the mean of 39 observations of motor arrest in a single animal across a single imaging session. The error bars represent the 95% confidence interval. One-way ANOVA was used to assess the statistical significance of the response [30], while Linear Contrast analysis was used to reject the dominance of a linear trend in the data [30], suggesting at least
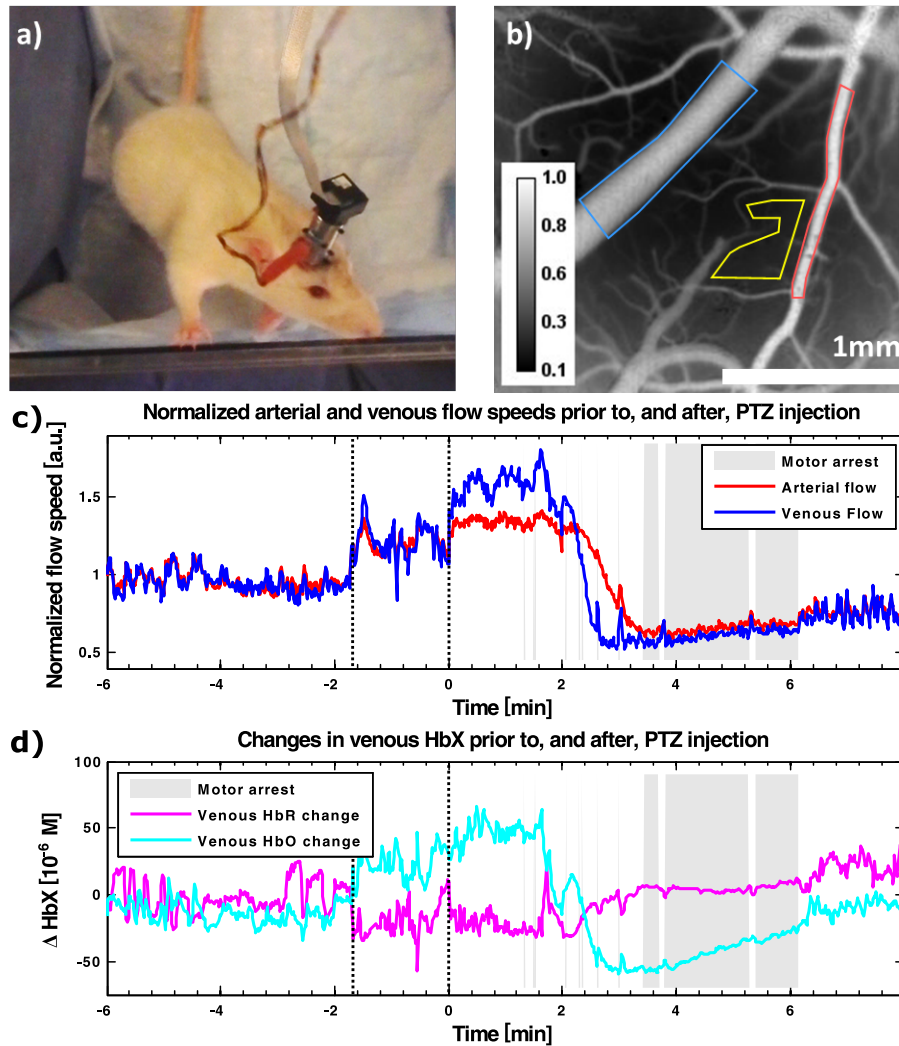
Fig. 3. a) A photograph of the rat exploring the imaging chamber with the skull-mounted imaging system. b) An LSCI-derived blood flow map. Inset: flow speed intensity scale, in arbitrary units. Highlighted are three areas used for generating the time courses for subsequent vascular analysis: vein (blue), artery (red), and the parenchymal region (yellow). c) Time course of the normalized blood flow speeds in the artery (red) and vein (blue). d) Time course of changes in HbO (cyan) and HbR (magenta) in the vein. Two time points are marked with vertical dashed lines: $t = -1.8$ min marks the time when the animal was picked up from the imaging chamber, and $t = 0$ min marks the time of PTZ injection.

one significant extremum point. We defined the magnitude of a hemodynamic change as the difference between the extremum point in a time course and the baseline prior to the motor arrest, taken as the mean of the first three time points (10-8 seconds prior to an event). The results of the analysis of the time courses in Fig. 5 is summarized in Table 1. The time courses suggest that the hemodynamic response prior to motor arrest is characterized by an increase in vascular flow (Figs. 5(a,b)). The maximum increase in flow precedes onset of motor arrest by 3 sec. Following this increase, we observe a reduction of the vascular flow speeds during motor arrest. Changes in
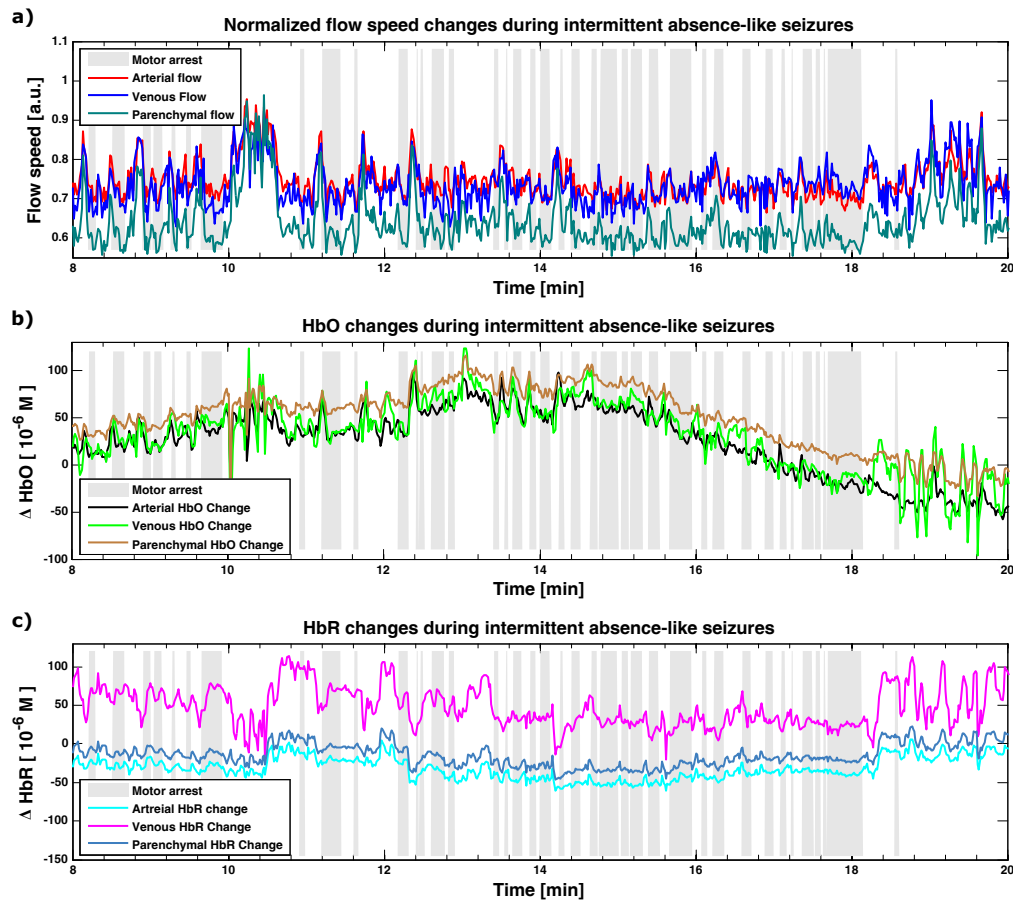
Fig. 4. Time courses of hemodynamic response between 8 and 20 minutes following PTZ injection. a) Changes in normalized blood flow speeds in artery (red), vein (blue), and parenchymal region (dark green). b) Changes in HbO in the artery (black), vein, (green) and parenchymal region (brown). c) Changes in HbR in the artery (cyan), vein (magenta), and parenchymal region (dark blue).

parenchymal flow speeds was not significant. The events are also characterized by an increase in HbO concentration in all three regions we examined (Figs. 5(d-f)). There is a phase delay between the arterial, venous, and parenchymal responses, where the venous response lags the arterial and parenchymal response by 2 sec. This increase in HbO is coupled with a decrease in venous HbR concentration (Figs. 5(g-i)). The change in arterial HbR concentration is not significant, while the change in the parenchymal HbR concentration are much smaller than the changes in the vein.

To further illustrate the hemodynamic changes taking place prior to, and immediately after, motor arrest onset, we show the mean changes in the flow speeds, HbO, and HbR across the full ROI in Fig. 6. Every tile shows the mean change in the hemodynamic quantity across the same time scale as the horizontal axis in Fig. 5 (the first and last tiles, at $t = -10$ sec and $t = 9$ sec, were removed to improve visual clarity in print). Flow and HbR changes were concentrated in the vessels, while changes in HbO were more homogenous across the ROI. This is consistent with our understanding of mechanisms of NVC [4], whereby neuronal activity triggers the release of vasoactive agents, leading to over-supply of HbO and increase in flow. There is no heterogeneity
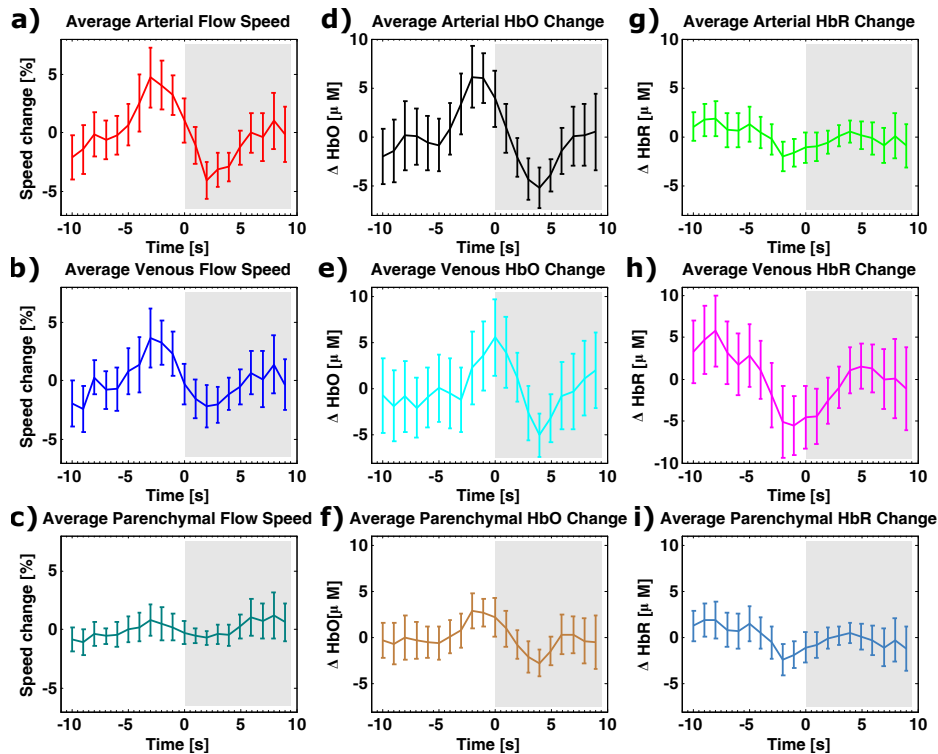
Fig. 5. Mean changes in hemodynamic activity prior to, and immediately after, onset of motor arrest. All curves represent average time courses of 39 seizures during a single imaging session in a single animal, superimposed on a time scale where $T = 0$ sec is the seizure onset, characterized by motor arrest. Error bars represent 95% confidence bounds on the mean standard error. a) arterial flow speed, b) venous flow speed, c) parenchymal flow speed, d) arterial HbO concentration, e) venous HbO concentration, f) parenchymal HbO concentration, g) arterial HbR concentration, h) venous HbR concentration, i) parenchymal HbR concentration

Table 1. Mean changes in monitored hemodynamic parameters during motor arrest in a single imaging session in a single animal.

Quantity	$F\,(19, 760)$	p	$F_{contrast}\,(1, 760)$	$p_{contrast}$	Change
Arterial Flow	5.44	1.22×10^{-12}	1.53	0.22	$5.9 \pm 1.7\,\%$
Venous Flow	3.02	1.66×10^{-5}	0.25	0.62	$5.0 \pm 1.6\,\%$
Parenchymal Flow	1.16	0.28	4.45	0.035	$2.1 \pm 1.2\,\%$
Arterial HbO	4.32	2.99×10^{-9}	0.44	0.51	$7.2 \pm 2.4\,\mu M$
Venous HbO	1.86	0.014	2.67	0.94	$6.7 \pm 3.0\,\mu M$
Parenchymal HbO	1.91	0.011	3.06	0.08	$3.2 \pm 1.5\,\mu M$
Arterial HbR	1.57	.056	21.9	3.46×10^{-6}	$0.3 \pm 1.3\,\mu M$
Venous HbR	2.91	3.29×10^{-5}	0.31	0.57	$-10.1 \pm 2.8\,\mu M$
Parenchymal HbR	1.74	0.028	1.17	0.28	$0.2 \pm 1.4\,\mu M$

to the response in the parenchymal region, suggesting the activity was not focal to the location we observed. Furthermore, the changes in HbR concentration suggest that the area in the ROI corresponding to the artery follows the same change as the parenchymal region. This is also corroborated by the very similar traces in Fig. 5(g,i). The most prominent changes in HbR are
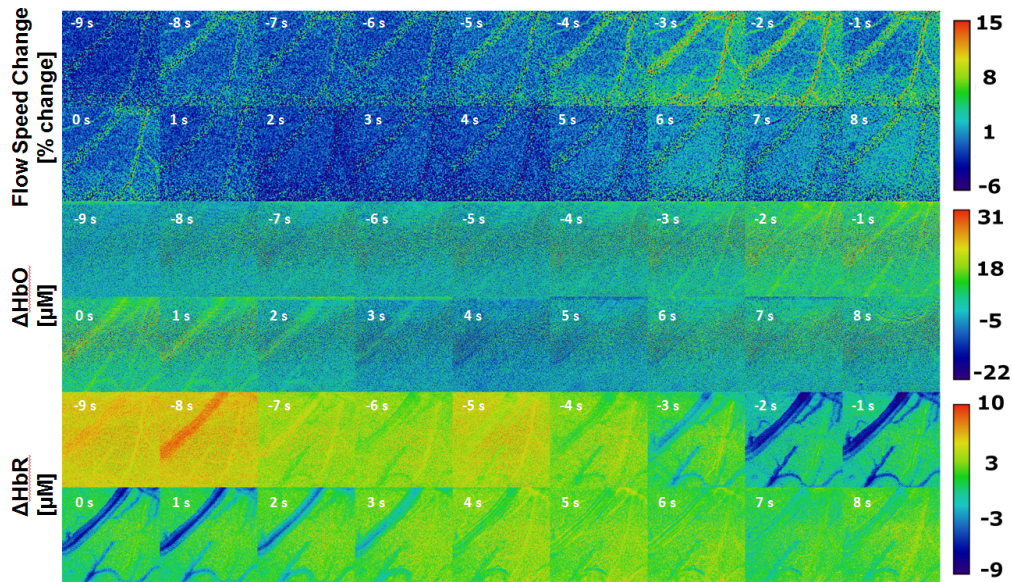
Fig. 6. Mean changes in the flow speeds (top two rows), HbO (middle two rows), and HbR (bottom two rows) across the full ROI. Each tile corresponds to a time point on the horizontal axis in Fig. 5, in seconds. $t = 0$ s correspond to onset of motor arrest, coinciding with the shaded gray region in Fig. 5. The first and last tiles, at $t = -10$ s and $t = 9$ s, respectively, were removed to improve visual clarity in print. The figure represents a single imaging session in a single animal.

clearly seen in the veins. This is expected, since veins drain the blood downstream of neuronal activity, after most oxygen exchange had taken place.

4. Discussion

We presented a device and method for longitudinal imaging of brain hemodynamics in awake, freely-behaving rats. The chronic cranial window allowed longitudinal imaging across 5 consecutive weeks (see Fig. 2), while the optical system provided robust, repeatable, high-quality imaging of cortical blood flow and oxygenation changes. The work presented here overcomes the limitations of previously published experiments, reviewed in section 1, of imaging in an acute session, which were typically restricted to several hours after cranial window placement. Our method enables measurement of the label-free biomarkers with higher dynamic range, as our imaging is unhindered by static scattering from the thinned skull and the dura matter. Furthermore, the complete removal of the dura layer in our approach overcomes the need to classify vessels as belonging to the cortex or the dura-matter, thus decreasing the ambiguity in interpreting the results. While our proposed device is heavier than the fiber-bundle based imaging system reported by Liu, *et al.*, [13] (15 g vs 1.5 g), the temporal resolution of the system presented here does not suffer from the need to perform temporal, as opposed to spatial, speckle analysis. As a result, high quality flow speed maps can be extracted at a higher frame rate (by averaging 8 frames instead of 240 frames).

We demonstrated awake imaging of an absence-like seizure model in a chronic setting, performed 6 weeks after the surgical implantation of the cranial window. We showed a correspondence between visually observed motor arrest associated with PTZ-induced seizures and statistically significant changes in the hemodynamic response. Misestimation of onset of PTZ-induced motor arrest by visual assessment of behavior increases the variance in our estimated

mean blood flow and oxygenation dynamics. Consequently, the responses presented in Fig. 5 likely underestimate the magnitude of hemodynamic changes associated with onset of seizure-like events. The true temporal dynamics could be more precisely estimated with concurrent optical and electrophysiological recordings in a future study, as we expect the electroencephalographic changes due to PTZ-induced seizures to precede the behavioural response.

We report an increase in vascular flow speeds prior to onset of motor arrest, which is qualitatively consistent with previously published characterization of PTZ-induced seizures [29]. This increase is likely attributed to increased metabolic stress due to hyper-synchronous activity that is associated with seizures, which we believe to commence prior to motor arrest. We also observe temporal phase delays between the flow, HbO, and HbR responses. The delay between the maxima of arterial and venous HbO changes can be partially attributed to the mean capillary-bed transit time for red blood cells, reported to be 1.5 s [31]. Changes in vascular flow speeds and blood volume have previously been shown to precede changes in hemoglobin composition [32–34] during functional activation. The delay we observe between maxima of flow changes and arterial HbO changes ($\sim$ 1 s) is in line with these prior reports. Interestingly, the increases we see in both flow and arterial HbO are short and transient, followed by a decrease in both. The reason for this is not easily explained by our understanding of PTZ-induced seizure-like events, and further studies are needed to better characterize the nature of this response. Potential explanation for this temporal dynamic lies in the location of the seizure onset zone. If the onset zone is located away from the imaged region, we would not observe the expected sustained increase in flow, but instead see only the transient effect. As such, the decrease in flow we see at motor arrest onset may be compensatory to a sustained increase in perfusion in a different cortical region. Similar observations of antagonistic activation away from the foci of neuronal activity have been previously reported in both optical [35] and blood oxygen-level dependent fMRI [36] studies.

We observed higher than average flow speeds and variability of oxygenation changes at time intervals when intermittent seizures were not present: at $t = 10 - 11.5$ min and $t = 18.5 - 20$ min in Fig. 4. We hypothesize that during these intervals the blood supply to the imaged region is recovering to its pre-PTZ injection baseline due to reduced demand from the seizure onset zone, which may be located outside the ROI. The rat did not appear to engage in abnormal movement patterns at these time intervals, which permits us to rule out stronger than average movement artifacts as the chief reason for these changes in the hemodynamic response.

Our current implementation has two main limitations: the fixed imaging area and the frame rate. Once the cranial window is implanted, only a 2 mm window can be imaged. In some models it may be desirable to image larger brain regions. This limitation can be addressed by reducing the aperture of the system to improve depth of field, and by placing a diverging lens after the VCSELs to increase the illuminated area on the cortex. These will enable imaging the full 6 mm-wide cranial window. The effective frame rate of $\sim$ 1 Hz, due to the need for averaging to gain sufficient SNR, may be limiting in some behavioral assays. The frame rate can be increased by dropping one or more channels, e.g. imaging flow speeds only, or by choosing an imaging sensor with faster acquisition rate.

Longitudinal imaging in awake rodents using miniaturized designs has been shown in other studies [37–42]. In these works, (single photon and two-photon) fluorescent labeling was used to provide optical contrast, and either a GRIN objective lens or a short fiber bundle was inserted into the cortex. Our device is compatible with single-photon fluorescence imaging, as there is sufficient space to insert an emission filter between the PBSC and the tube lens. The VCSELs used in the current work are compatible with dyes such as ICG and Evans Blue, commonly used by neurobiologists. The light source module can also be replaced with an appropriate light source (miniature LED or laser diode) for exciting Ca^{2+}-sensitive dyes and proteins.

5. Conclusion

In this work we have addressed the major limitations of imaging of cortical hemodynamics in awake rats: 1) we developed a system and method that allows for longitudinal imaging studies in rats, 2) we demonstrated chronic imaging of seizure activity in rats. Our work will enable future research into longitudinal studies of NVC in rat models of stroke and epilepsy, and could find application in pre-clinical drug testing.
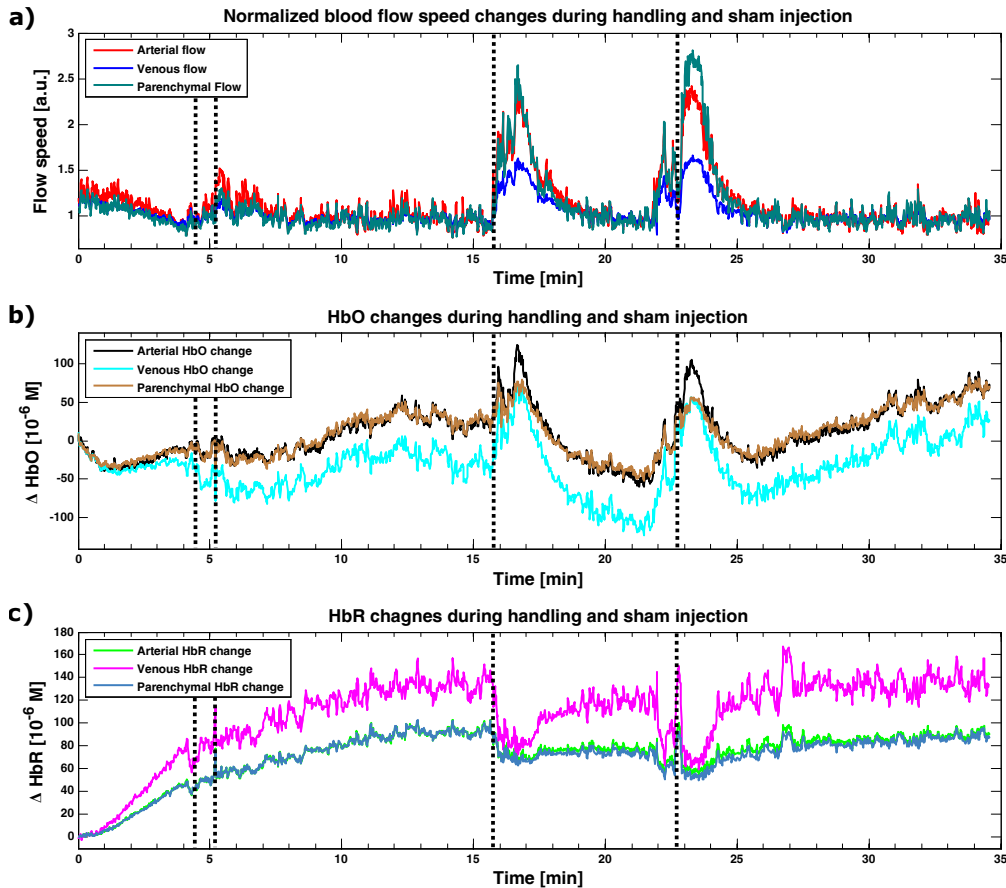
Appendix

Fig. 7. Hemodynamic response of a rat to handling and IP bolus injection. $t = 0$: isoflurance was turned off and the rat was allowed to recover. There are 4 vertical dashed lines that mark time points of interest: 4:20 min: rat regained consciousness, 5:15 min: rat was transferred to the imaging chamber, 15:45 min: the animal was picked up, removed from the chamber, and placed on its side. No injection took place. 22:50 min: 1 mL bolous saline was delivered via an IP injection. a) Changes in blood flow speeds, normalized to the mean baseline value, between $t = 7 - 12$ min. b) Changes in HbO. c) Changes in HbR.

Results in Fig. 7 suggest that the rat shows strong, global response to physical stimuli, characterized by a strong increase in blood flow speeds ($\sim$ 220% in artery, $\sim$ 50% in vein, $\sim$ 260% in parenchymal region), strong increase in HbO ($\sim$ 50 μM in a vein and artery, $\sim$ 20 μm in parencymal region), a decrease in venous HbR that is smaller than the decrease in HbO ($\sim$ 35 μM, indicating net influx of oxygenated blood during handling). Arterial and parenchymal

HbR responses are almost identical.